Modeling the Ultra-Wideband Outdoor Channel - Model Specification and Validation

Santos, Telmo; Tufvesson, Fredrik; Molisch, Andreas

Link to publication

Modeling the Ultra-Wideband Outdoor Channel: Model Specification and Validation

Telmo Santos, *Student Member, IEEE*, Fredrik Tufvesson, *Senior Member, IEEE*, and Andreas F. Molisch, *Fellow, IEEE*

Abstract—In this paper we establish a geometry-based stochastic ultra-wideband channel model for gas stations. We statistically describe the two-dimensional spatial location and power of clustered scatterers, and the shape of their visibility and shadowing regions. We also separately model the diffuse part of the impulse response (i.e., the part that cannot be explained by the scatterers' multipath components), and show that its amplitude fading statistics can be best described by a Weibull distribution with a delay dependent beta-parameter. A step-by-step implementation recipe demonstrates how the model can be built. Finally, we validate our model by comparing simulated and measured channel parameters such as the rms delay spread.

Index Terms—Geometry-based stochastic channel model (GSCM), outdoor, ultra-wideband (UWB), wireless propagation.

I. INTRODUCTION

ULTRA-WIDEBAND (UWB) communications is a technology capable of delivering high data rates over short distances. One possible application is the delivery of multimedia content to vehicles briefly stopping at locations such as gas stations (the focus of this work) or drive-thru restaurants. Such transmission scenarios have been dubbed *infostations* in the literature [1].

A fundamental prerequisite for analyzing the possible performance of such systems is an understanding of UWB propagation channels in outdoor gas station environments. In [2] we have described an extensive measurement campaign in such environments, concentrating on the measurement setup and data processing that yielded the 2D spatial position of relevant scatterers.

Based on those results, the current paper derives a detailed channel model. The model is novel both in the sense that many elements of its generic structure have not previously been proposed in the literature (these are listed in the next paragraph), and that no parameterized (quantitative) model has been previously proposed for the gas station scenario. The main purpose of the developed model is to enable system simulations of transmission in the considered environment.

A large number of generic channel models has been proposed in the literature [3]–[5]. In particular, for UWB channels, tap delay line channel models with regular tap spacing [6], [7], Saleh-Valenzuela-type channel models [8], [9], as well as geometry-based models [10] have been used. However, none of the existing generic modeling approaches is completely suitable to explain all the features of our measurement results. We therefore introduce a new model that bears some similarities to [10]–[12] in that it is also geometry-based, and considers discrete path components as well as diffuse components. However, we introduce several novel concepts for UWB channel modeling: (i) cluster "beampatterns" describing the directional dependence of the radiation emanating from a cluster, and (ii) shadowing regions that represent the large-scale attenuation of the LOS for certain TX/RX locations.

The remainder of the paper is organized as follows. First, in Section II we summarize our previous work, subsequently in Section III we describe the chosen modeling approaches and their motivations based on the measured data. Then, in Section IV we provide the values for all the model parameters and give a step-by-step formula to generate the channel impulse responses. In Section V the model validation is presented and in VI we wrap up the paper with the conclusions.[1]

II. MEASUREMENT CAMPAIGN AND POST PROCESSING

For the convenience of the reader, this section summarizes the measurement methodology and data postprocessing of our gas station measurement campaign; more details are given in [2].

The measurements were performed at two gas stations (scenario 1 and 2) near Lund, Sweden. At each of them, the positioning of the antennas was as follows: the antenna representing the BS was placed at the entrance of the gas station shop or near the top of one of the gas pumps, while the second antenna, representing the MS, was moved along a rail positioned at the sides of the gas pumps (the location where a vehicle is expected to stop or pass through). A single rail of measurements compromised 170 MS positions separated 0.048 m from each other, creating an *eight* meter virtual

---

[1]*Notation a)* The term *power*, is used throughout this paper referring to the dimensionless quantity of the received to transmitted power ratio defined as $P_o/P_i = |V_o/V_i|^2$. The ratio of received to transmitted complex voltages, V_o/V_i, is the quantity measured by the vector network analyzer (VNA). *b)* The terms TX (transmitter) or BS (base station), and RX (receiver) or MS (mobile station) are used interchangeably throughout the text. *c)* In order to maintain self-consistency of the definitions for the different statistical models, we refer to the pdfs as defined in the book by Papoulis [13] unless specifically indicated otherwise.

array. During the measurement of each array, BS and scatterers did not move; furthermore the MS did not move during the measurement at one particular MS position, so that the channel was completely static. Furthermore, in each of the two gas stations, we had two BS positions combined with four MS rail positions, resulting on a total of $2 \times 2 \times 4 \times 170 = 2720$ frequency responses measured in the two scenarios. The transfer functions of the channels were measured by means of a VNA, configured to measure the S_{21} parameter of $N_f = 1601$ regularly spaced frequency points, covering from 3.1 to 10.6 GHz. The antennas were SkyCross SMT-3TO10M-A, chosen for their *approximately* omnidirectional radiation pattern in the horizontal plane (a polar measurement plot of the antenna's radiation pattern can be found in [14, Fig. 4.4]). No attempts were made to eliminate the influence of the antennas from the measured data; they are therefore *ipse facto* included in the proposed model.

The data post processing phase consisted of two main steps

- *Scatterer detection* – In this step we used a novel channel estimation method, which takes as input all the 170 frequency responses of a single eight meter virtual array, and identifies the scatterers by means of successive cancellation.[2] The method makes use of (i) the fact that an MPC is visible from several consecutive (on the rail) MS positions (also referred to as *visibility region*) and (ii) the assumption that only *single-scattering* processes occur, in order to find the spatial location of the scatterer. In addition, the transfer function of each MPC is considered to decay with frequency according to the power-law f^{-m}, where m is common to all MPCs and is estimated as explained in Section III-I.

  Each one of the detected scatterers is then characterized by its 2D coordinates, visibility region and received power of its associated MPC at the different MS positions. The figures in Section IV provide a more visual interpretation of these concepts, e.g., one given point (scatterer) in Fig. 8 is mapped to a time-varying component of the impulse responses in Fig. 9.

- *Clustering of scatterers* – This method assigns each scatterer to a cluster, where a *cluster* is defined to be a group of scatterers located at similar points in space. The clustering is based on a the modified K-means approach of [15].

Further analysis showed that scatterers belonging to the same cluster reflected radiation in a similar way, which can be well described by *beampatterns* pointing into specific directions.

III. CHANNEL MODEL DESCRIPTION

This section is devoted to the description of the channel model concepts. We start with the general overview and qualitative comments, and then proceed, with a more comprehensive and quantitative description of each of the modeling approaches in separate subsections.

---

[2] A *scatterer* is here defined to be a point in a 2-dimensional space that reflects power from the TX to the RX antenna. A *multipath component* (MPC) is the name given to the signal that arrives at the RX from the scatterer.

Our model is fundamentally a geometry-based stochastic channel model (GSCM) [16]. This means that each realization of the channel is obtained by first choosing the location and power of the scatterers stochastically (creating a static geometrical map). Then the impulse response of the different MS positions is obtained by means of a simplified ray tracing where the different MPCs are superimposed at the receiver.

A single channel realization is characterized by a geometrical map, composed of static scatterers, from which several impulse responses (from the different MS positions) can be calculated.

A fundamental assumption of our model is that we only consider single-scattering processes. While being a simplification, single-scattering was found to describe the greater part of the channel impulse response. This is evidenced by the fact that the locations of the clusters of scatterers, which are determined *under the assumption of single-scattering*, could almost always be mapped to physical objects in the measured scenarios, e.g., gas pumps and pillars. The dominance of single-scattering was thus found to be a distinct property of these scenarios. While multiple-scattering processes still exist, they are associated with radiation carrying only low power. We include those contributions in the diffuse component.

A general equation for the transfer function of the modeled channel is thus

$$H_n\left(f\right) = \left(\overbrace{S_{\mathrm{LOS},n}(f)}^{I} + \overbrace{\sum_k S_{n,k}\left(f\right)}^{II} + \overbrace{\mathcal{F}\left\{D_n(\tau)\right\}}^{III} \right) \overbrace{\frac{f^{-m}}{F}}^{IV}.$$
(1)

The index n identifies the different MS positions, such that $n = 1, \ldots, N_{\mathrm{MS}}$. The main constituents of channel model are:

- *I* – the *quasi-LOS component*, with transfer function $S_{\mathrm{LOS},n}(f)$, which is calculated deterministically from the distance dependent path-loss and is also affected by the shadow effects,

- *II* – the *discrete multipath components (MPC)*, with transfer functions $S_{n,k}\left(f\right)$, which are derived from the spatial position of the scatterers, the radiation pattern of the corresponding clusters, and the path-loss,

- *III* – the *diffuse component*, which is defined by a deterministic large-scale attenuation superimposed on a purely statistical small-scale fading ($\mathcal{F}\left\{\cdot\right\}$ stands for the Fourier transform operation) and

- *IV* – the *frequency dependency*, which models the frequency dependence of the *average* magnitude of the transfer function that occurs in UWB channels [3] (the use of this term also denotes that we assume all MPCs to have the same distortion). F is a normalization factor used to ensure that f^{-m} does not affect the frequency-integrated power of the channel's transfer function.

The detected scatterers were found to be arranged in clusters and this fact needs to be reflected by the model. We therefore distinguish between the inter-cluster properties (e.g., the statistics of the cluster center locations), and the intra-cluster properties, i.e., the location of scatterers *within* a cluster.

In the course of the model development, we often had to establish which pdf best describes a particular model parameter. For this model selection, we followed the recent

work of Schuster [17] and employ the Akaike Information Criteria (AIC), or more specifically, its normalized version, the Akaike weights. This was found to be preferable to the more traditional goodness-of-fit (GOF) tests, which have subjective significance levels. The basic idea behind AIC is "...the maximization of the expected log likelihood of a model determined by the method of maximum likelihood" [18].

Note that in this section, we present only the functional shape of the pdfs of the scatterers. The actual numerical values parameterizing those pdfs will be presented in Section IV.

A. Type and Number of Clusters and Scatterers

Since the BS was always placed on a structure of large dimensions (e.g., a wall or pillar), we found that one cluster surrounding the BS always existed. This cluster was characterized by having a larger number of scatterers than the remaining clusters: on average the number of scatterers per BS cluster was 115 and for non-BS clusters it was 30. For this reason, we model these two types of clusters separately.

The number of clusters, N_{cl}, was found to be well modeled by a Poisson distribution in accordance with the literature [9]. However, this analysis was based on a very small population of independent samples, only 16, which can be deemed insufficient for a good statistical analysis. The number of scatterers per cluster, N_{sc}, could best be described by a discrete version of the Gaussian distribution truncated to positive outcomes.[3]

B. Cluster Positions

We model the distribution of the cluster coordinates (i.e. the coordinates of the cluster center) as a two-dimensional uniform distribution. This is clearly an oversimplified picture, since the layout of a gas station (lines of gas pumps, etc.) gives rise to a more regular structure. Nevertheless, for want of a better model, we employ this uniform distribution in the following, while noting that the cluster location can be adapted based on future measurements, or even based on location-specific geometrical information, in the spirit of [10].

In the model, the clusters are only allowed to exist within a finite area surrounding the BS and MS antennas. The delimitation of this area is found from the delay of the furthest cluster detected from the measurements, which was $\tau_{c,max} = 128$ ns. Thus, the cluster location pdf is uniform within an ellipse whose foci are the BS and center MS position, being defined as,

$$f_{uniform}\left(x', y'\right) = \begin{cases} \frac{1}{\pi \alpha_e \beta_e} & , \frac{x'^2}{\alpha_e^2} + \frac{y'^2}{\beta_e^2} \leq 1 \\ 0 & , \text{otherwise} \end{cases}. \quad (2)$$

The auxiliary coordinate system (x', y') is used here to facilitate the formulation of the distribution. The x'-axis is oriented along the line that connects the BS to the center MS position, and the origin $(x', y') = (0, 0)$ lies on the mid point of that line. The semimajor axis of the ellipse is $\alpha_e = \tau_{c,max}c/2$ and the semiminor axis is $\beta_e = \sqrt{\alpha_e^2 + d_{\text{foci}}}$,

---

[3]Due to the lack of a physical reasoning or existing literature that would indicate a certain statistical description for these parameters, we compared the histogram of the data with several distribution and chose the one that best matched the data.

where d_{foci} is the distance between the two foci of the ellipse and c is the speed of light in vacuum. Fig. 8 shows the *allowed cluster area*, where the foci are the BS and the center MS position.

C. Scatterer Positions Within a Cluster

From inspection of plots of scatterer locations, we noted that the density of scatterers decreases with distance to the cluster's centroid. We could furthermore see by inspection that the density is rotationally symmetric, which suggests the use of a bivariate pdf for the two spatial coordinates (x_s, y_s) around the centroid. The pdfs along the two coordinate axes are assumed to be uncorrelated with the same variance, such that the scatterers will be equally spread around the cluster centroid.

The next step is to identify a good distribution to describe the variations with the x_s and y_s coordinates. To this end, we tested the bivariate Gaussian and Laplace distributions. The main difference between the two candidates is that the Laplacian is highly peaked at the origin and falls off less quickly than the Gaussian at large distances from the centroid. The model selection was based on the Akaike weights, which were computed for both distributions and showed the bivariate Laplace distribution to be the better fit to the measurement results. This distribution is defined as [19],

$$f_{Laplace}\left(x_{s'}, y_{s'}\right) = \frac{1}{\pi \kappa} K_0 \left(\sqrt{\frac{2}{\kappa}\left(x_{s'}^2 + y_{s'}^2\right)} \right), \quad (3)$$

where κ is the parameter of the distribution and $K_0(\cdot)$ is the zero-th order modified Bessel function of the second kind. Note that this is the distribution of the coordinates within a cluster, the true coordinates (with the BS as the origin) are $(x_s, y_s) = (x_{s'} + x_c, y_{s'} + y_c)$, where (x_c, y_c) are the cluster centroid coordinates.

D. Scatterer's Power

On average, the power received via the different scatterers decreases with the *run-length* of the signal, namely following a power law

$$P_{\text{PL}}\left(d_{t:s:r}\right) = P_0 \left(d_{t:s:r}/d_0\right)^{-n_{\text{PL}}}. \quad (4)$$

Here, n_{PL} is the path-loss exponent, $d_{t:s:r}$ is the distance from the transmitter, through a given scatterer to the receiver, and P_0 is the mean power at the reference distance d_0. The fit of d_0 and P_0 to the measurement results was done in the least-squares sense, based on all the MPCs excluding the direct LOS component.[4] Since for very small distances, the above equation would stop being valid (as $d_{t:s:r} \to 0, P_{\text{PL}} \to \infty$), only $d_{t:s:r} \geq d_0$ are considered, where the reference distance is $d_0 = 1$ m.

The power law described above describes only the *mean* power of the MPCs; however, individual components show a variation around this mean. These power deviations, p_s, were found to be well modeled by a log-normal distribution,

---

[4]The path-loss of the LOS component is modeled separately in Section III-G since it does not include an interaction with scatterers.
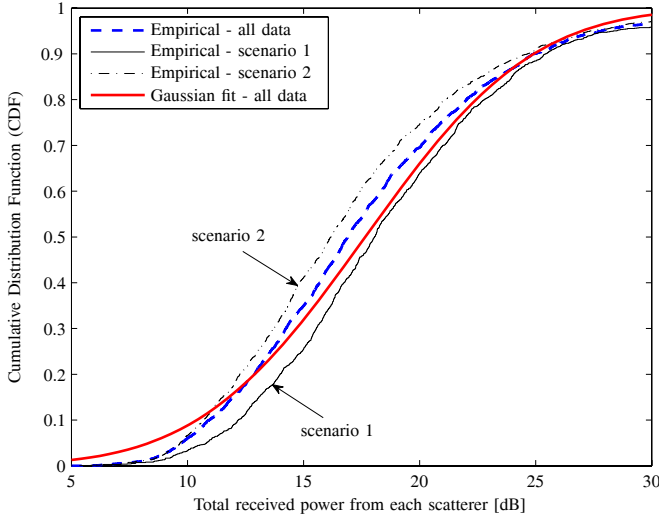
Fig. 1. Log-normal total received power variations of the scatterers after path-loss compensation. The two thin lines correspond to the data from scenario 1 and 2 separately.
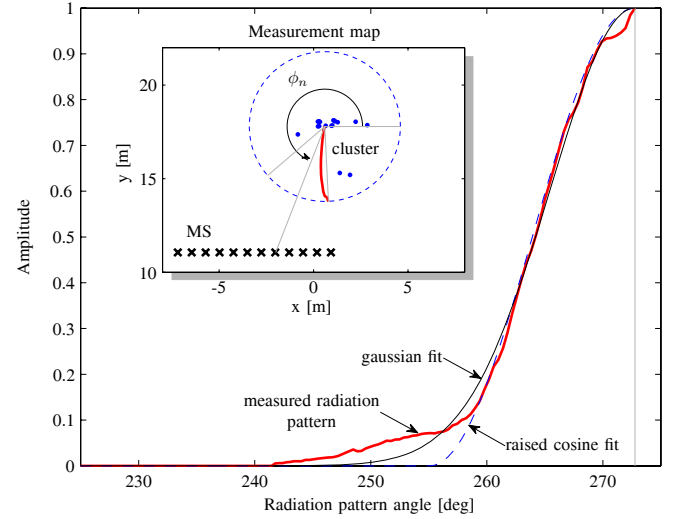

Fig. 2. Example of a measured cluster's radiation pattern with the corresponding Gaussian and raised cosine fits. The small figure shows the geometrical map containing the position of the cluster and all the MS positions, plus the measured radiation pattern plotted in polar coordinates.

which when plotted in dB scale is transformed into a Gaussian distribution. Their empirical CDFs and corresponding Gaussian fit are shown in Fig. 1. The match between the theoretical and measured curves is not perfect, in particular on the distribution tails (this mismatch can better be analyzed by means of a quantile-quantile plot), regardless, for simplicity sake we consider the lognormal distribution suitable to model the power variations.

It is noteworthy that this power law (plus lognormal deviations) is different from the conventional power law for the pathloss [20]. The conventional model ascribes a d^{-n} law to the *total* received power (not to the MPC powers, as in our case), and furthermore defines d as the distance between transmitter and receiver, not the runlength of the signal.

E. Visibility Regions of Clusters

From the measurements, we observed that specific scatterers could not be observed at all the measurement positions of the MS. Most often, a given scatterer was visible only if the MS was in a certain region (called visibility region). The transitions from being visible to not being visible (as the MS position changed continuously) were sometimes abrupt and on other occasions gradual.

The concept of visibility regions was introduced (for conventional wideband channels) by the COST259 Directional Channel Model [21]–[23]. It defines regions in space associated with a certain scatterer cluster such that a corresponding cluster becomes visible if the MS happens to be within the region. It also provides a transition function to describe the activation of the cluster when the MS enters the visibility area. An alternative approach was formulated in [24], using not the spatial but rather the angular domain: each cluster is ascribed an angle-dependent radiation pattern. In the currently proposed model we choose the latter approach. This is in line with our initial study of the measured clusters, when we looked at their angular radiation pattern.

As reported at the end of Section II, these patterns were found to have *beam*-like shapes. We tested two candidate

shapes to describe the radiation patterns that also have *beam*-like properties, namely a (truncated) Gaussian and raised-cosine functions. The main difference between them is that the latter has a limited width beyond which all angles have zero response, while the former has non-zero values for all angles. Fig. 2 shows an example of a measured radiation patterns and the corresponding fits. To choose the best shape parameters we minimized the mean square error (MSE),

$$\nu_{opt} = \arg\min_{\nu} \frac{1}{N} \sum_{n=1}^{N} \left(R_{\phi_n} - R'_{\phi_n}(\nu) \right)^2,$$

where R_{ϕ_n} is the measured radiation pattern[5] after path loss compensation, $R'_{\phi_n}(\nu)$ is the shape to be tested, N is the number of measurement points and ϕ_n is the angle between the horizontal line passing through the cluster and the line connecting the cluster to the n-th MS position. The variable over which the minimization is performed is ν. For the Gaussian case, 2ν is the pulse width at an amplitude of $1/e$, and for the raised cosine case, ν is the pulse width at an amplitude of $1/2$. Both shapes plus measured radiation pattern are normalized to a maximum amplitude of 1 and centered at the angle providing amplitude. By fitting these two shapes to all the 52 measured clusters, we found that the average MSE for the Gaussian was 3.35×10^{-2} and the average MSE for the raised cosine was 3.62×10^{-2}. Hence, the Gaussian shape is superior in the MSE sense, although the difference between the two is small. The Gaussian shape is defined here as

$$V(\phi) = \exp\left(-\frac{(\phi - \phi_0)^2}{\nu^2} \right), \qquad (5)$$

where $V(\phi)$ is only defined for $\phi_{min} \leq \phi \leq \phi_{max}$, and the limits are given by the cluster and MS position as illustrated in Fig. 3. The shape is controlled by the parameters, ϕ_0 ($\phi_{min} \leq \phi_0 \leq \phi_{max}$) and ν ($\nu > 0$). The former specifies the

---

[5]The measured radiation pattern of a cluster is found from the averaging of all the individual scatterers' patterns that constitute that cluster, [2].
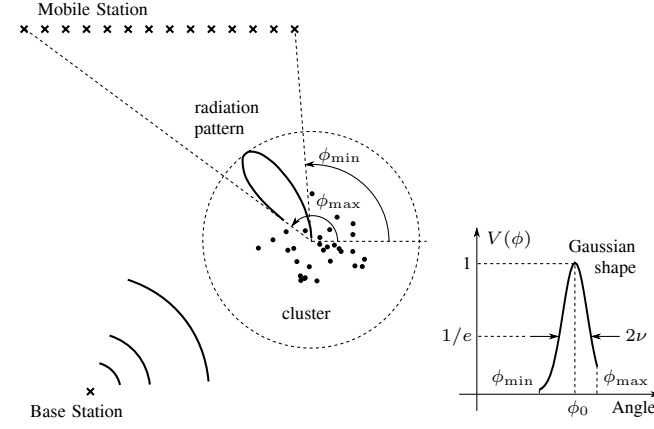
Fig. 3. Definition of visibility region from the cluster's radiation pattern. On the left, a map view representation with the radiation pattern in polar coordinates, and on the right, the same in cartesian coordiantes.
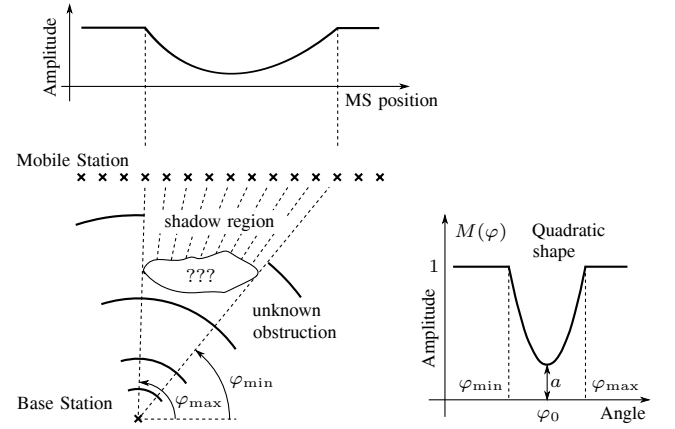

Fig. 4. Definition of the shadow region as a quadratic shape in the angular domain. The plots show the normalized received signals strength without the influence of path loss. The upper plot, in the *MS position* domain and the lower one, in the *angular* domain.

main direction of the radiation beam, modeled as uniformly distributed within the available angular range, and the latter gives information about how focused the beam is, and is assumed to follow a log-normal distribution.[3][6] The parameters for these pdfs were estimated from the 52 measured clusters.

Our definition also intrinsically states that all created clusters are visible in *some* region. This is reasonable, since the non-visible clusters are impossible to detect during measurements, and there is no information about them. Finally, assigning a radiation pattern to a cluster means that we expect all scatterers from that cluster to share the same radiation pattern.

F. Shadow Regions

In the measured scenarios, there were locations at which the LOS between the transmitter and receiver antennas was obstructed. A simple analysis of the data revealed that, in some cases, the shadowing by a single object was responsible for a loss of 13 dB of the overall impulse response power. Simply distinguishing between "LOS" and "NLOS" cases, as often done in the literature, does not provide the important information about the dynamic channel evolution as an MS moves from a shadowed to an unshadowed region. There is therefore a need for *shadow regions* in the model.

The above mentioned obstruction was generally due to gas pumps, pillars and/or other objects of comparable size. This obstruction was found to affect all the multipath components belonging to the BS cluster but not the remaining multipath components. Accordingly, in the present model, shadow regions are assigned to BS clusters while visibility regions, Section III-E, are assigned to non-BS clusters.

As explained in [2, IV-B], diffraction theory provides a good explanation for specific shadowing effects. However, introducing diffraction equations into our model would make it far too complex. Furthermore, from our measurements, we were only able to identify 18 shadow regions, which is insufficient to build a statistically relevant yet detailed model for the corresponding signal variations. Due to these

reasons, we selected a very simple quadratic shape to an angular shadowing region (beampattern) to describe the signal variations, which captures the main effect of shadowing, namely the reduction of the signal amplitude behind objects. More precisely, we define the shadow region, cf. Fig. 4, by the mask,

$$M(\varphi) = \begin{cases} (1-a)\left(2\frac{\varphi-\varphi_0}{\Delta\varphi}\right)^2 + a & , \varphi_{\min} \leq \varphi \leq \varphi_{\max} \\ 1 & , \text{otherwise} \end{cases}. \tag{6}$$

The shadow region angular width is defined as $\Delta\varphi = 2(\varphi_{min} - \varphi_0)$, where φ_0 is the mid-angle between φ_{max} and φ_{min}. The parameter a is used to control the maximum signal loss which happens when the MS is exactly behind the object. The term *mask* is used here because (6) will be applied, as a multiplicative mask, to the LOS component (15) and to the multipath components belonging to the BS cluster in (14). The shadow effect is also illustrated in Fig. 9.

The parameter φ_0 is modeled as a random variable that is uniformly distributed over the available angular range and a and $\Delta\varphi$ are constants estimated from the measurements of the 18 available shadow regions.

Finally, the number of shadow regions $N_{sh,8}$, found from our 8.11 m virtual array, is modeled by a Poisson distribution.[3] The statistical description of $N_{sh,8}$, implies that a specific MS route can have multiple or no shadow regions at all. The density of shadow regions can be found by normalizing the number of shadow regions by the array length, $N_{sh,8}/8.11$.

G. Line-Of-Sight Power

The power of the LOS component as a function of distance also needs to be quantified. By LOS component we mean the UWB pulse that propagates from one antenna to the other without interaction with any obstruction. The standard model suggests that the LOS power follows a power-law

$$P_{\text{LOS}}(d_{t:r}) = P_0 (d_{t:r}/d_0)^{-n_{\text{LOS}}}, \tag{7}$$

where P_0 is the LOS power at the reference distance d_0, chosen to be $d_0 = 1$ m, and $d_{t:r}$ is the distance between the transmitter and a given receiver position.

---

[6]It should be noted that our approach of modeling the shape parameter ν as a random variable, leads to some level of over-fitting bias, since the shape itself was chosen based the MSE criterion using to the same measured data.

It is well known that the free space path-loss for spherical waves in the far-field is proportional to the inverse of the distance squared. However, estimates from the measured data gave $n_{\text{LOS}} = 1.67$. This result indicates that the LOS component might be influenced by other components that cannot be resolved from the LOS component because their delays are too similar.

H. Diffuse Multipath Component

The discrete components associated with particular scatterer locations cannot explain all the power experimentally observed in the impulse responses. The remainder can be described as diffuse multipath component (DMC) and it often results from processes like multiple-scattering, rough surface scattering and diffraction around objects. Since these components have low power, are numerous and originate from all directions surrounding the antennas, an attempt to model them on a geometrical basis would result in an overly-complex channel model; we therefore choose a purely stochastic description.

The data from which we extract the DMC characteristics is the remainder of the impulse response *after* the application of the scatterer detection method, briefly described in Section II. In every step of the method, discrete scatterer contributions were detected and subtracted, so that the remaining *cleaned* channel is assumed to be free of specular components, with only the DMC being left. The detection method may also have generated cleaning artifacts due to the assumption that all multipath components have the same frequency dependence; these artifacts become subsumed into the modeled DMC.

It is a common assumption that the DMC power, on average, decays exponentially as a function of delay, starting immediately after the LOS component (zero excess delay) [25]. Hence, a sufficient description of the average behavior of the DMC power is obtained by estimating its decay exponent (or correspondingly, its rms delay spread) and its level of power at zero excess delay. In order to capture all the dependencies of the DMC, we model these two parameters as a function of the distance between the antennas, $d_{t:r}$.

While the rms delay spread dependence on the distance has been previously studied for full impulse responses [26], we apply the same principles to the DMC only, c.f. Fig. 5. The large-scale DMC power is then fully described by,

$$D_{\text{LS}}(\tau) = \begin{cases} D_{\tau_{\text{LOS}}}(d_{t:r}) \exp\left(-\frac{\tau - \tau_{\text{LOS}}}{\tau_{\text{RMS}}(d_{t:r})}\right) & , \tau > \tau_{\text{LOS}} \\ 0 & , \tau \leq \tau_{\text{LOS}} \end{cases} \quad (8)$$

where the power at zero excess delay, in linear scale, is defined as,

$$D_{\tau_{\text{LOS}}}(d_{t:r}) = D_0 \left(d_{t:r}/d_0\right)^{-n_{\text{D}}} \quad (9)$$

and the rms delay spread of the DMC is,

$$\tau_{\text{RMS}}(d_{t:r}) = \tau_0 \left(d_{t:r}/d_0\right)^{n_{\text{RMS}}}. \quad (10)$$

The parameters D_0, n_{D}, τ_0 and n_{RMS}, were estimated from all the 2720 *cleaned* channel responses.

We next analyze the amplitude statistics of the DMC's small-scale fading, as a function of the excess delay. The 170 different MS locations constitute the statistical ensemble from which we can obtain the pdf, while the delay is considered
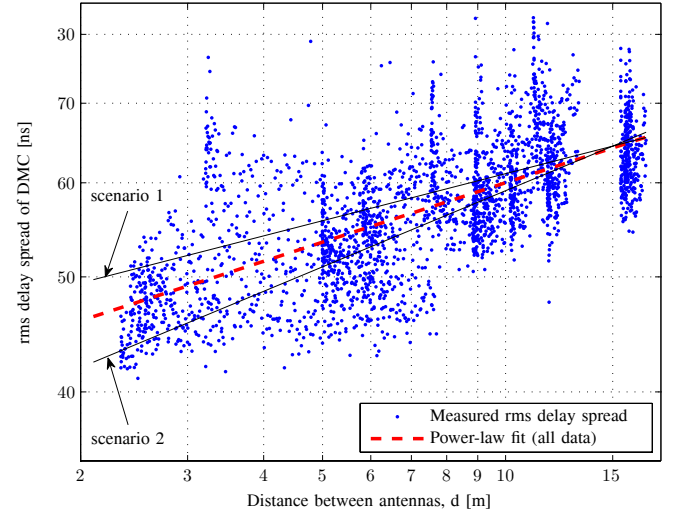

Fig. 5. Exponent of the diffuse multipath component versus distance. The thin lines show the fit to the data from scenario 1 and 2 separately.
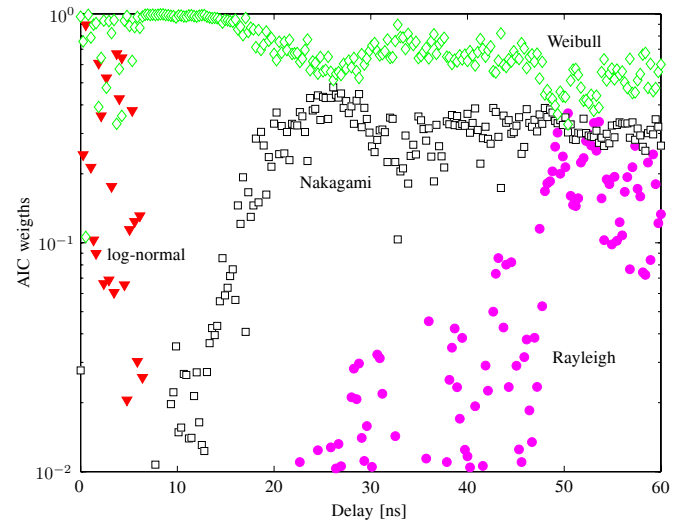

Fig. 6. Akaike weigths of the four candidate distributions to describe the DMC small-scale variations as a function of delay.

a deterministic parameter on which the pdf can depend. We note that for each delay value we normalize the signal such that it has unit mean power. Then, five candidate distributions were considered for the amplitude pdf, whose parameters were calculated based on ML estimates: log-normal and Rayleigh by their closed form expressions, Rician by a grid search maximizing the log-likelihood function with a step size of 10^{-4}, Nakagami by an approximate ML estimator [27] and Weibull by a numerical method finding the zero of the partial derivatives of the log-likelihood function with an error below 10^{-5} [28]. Again we use the Akaike weights for the model selection. Fig. 6 shows the weights (on a logarithmic scale) versus delay.[7]

From the figure, it can be observed that for small excess delays, both Weibull and log-normal are the preferred distributions. Then, with increasing delay, the log-normal distribution starts to perform worse, while Nakagami and Weibull are

---

[7]Since the Rician weights were very similar to the Rayleigh ones, these are not shown in the figure for clarity.
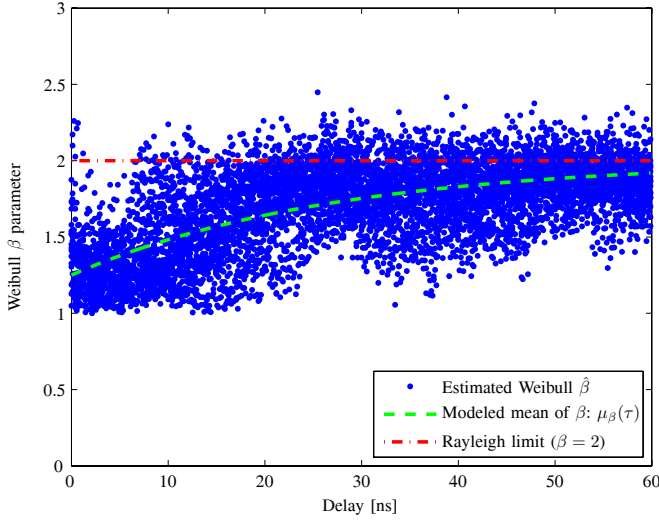
Fig. 7. Estimated Weibull $\hat{\beta}$ parameter as a function of delay and corresponding modeling.

the best. Also with increasing delay, the data progressively becomes more "Rayleigh-like". Since the Weibull distribution is (among the) best fit over the whole delay range, we choose it to model the small-scale fading of the DMC amplitude, $D_{ss}(\tau) \sim f_{Weibull}(\alpha, \beta(\tau))$.[8]

The Weibull distribution is defined by the *scale parameter* α and the *shape parameter* β, where the latter one is comparable to the m-parameter of the Nakagami distribution. Fig. 7 shows the estimated values of β. The values of β below 2 represent a fading worse than Rayleigh.[9] From Fig. 11, one can observe that indeed the data approaches Rayleigh with increasing delay $\beta \to 2$ as $\tau \to \infty$. To capture the essence of this behavior, we empirically model the β parameter as a delay dependent variable defined by,

$$\beta(\tau) = 2 + \frac{u-2}{(\tau+1)^v}. \tag{11}$$

Here, u defines the mean value of β at $\tau = 0$ and v controls the curvature of the line as it tends to $\beta = 2$. The value of both the parameters was estimated by minimizing the mean square error from the data in Fig. 7. At first glance, one might attribute the Rayleigh-like amplitude statistics at large delays to measurement noise; however, the power of the DMC at 60 ns was, on average, calculated to be 15 dB above the noise power, and therefore, the noise influence in $\hat{\beta}$ is minimal. The bias of the estimator for the Weibull parameters in the presence of noise, considering the 170 samples, was computed through simulations to be below 0.025 for all delays and thus neglected. Finally, the Weibull α parameter can be deterministically calculated since it is a function of both β and the mean power. Since the mean power was normalized to one, it here simplifies to,

$$\alpha = \beta \left[\Gamma (1 + 2/\beta) \right]^{\beta/2}, \tag{12}$$

where Γ is the Gamma function. Regarding the phase of the

---

[8]The τ dependence is explained in the following paragraphs.

[9]A factor possibly contributing to the worse-than-Rayleigh fading is the scatterer detection method that also canceled part of the diffuse component and introduced ghost components, creating an additional artificial fading.

DMC taps θ_{DMC}, all our tests revealed it to be uniformly and independently distributed from 0 to 2π.

I. Frequency Dependent Decay

Finally, we have also studied the frequency dependence of the pathloss, which is one of the distinguishing characteristics of the UWB channels compared to narrow-band ones. This characteristic requires us to use a frequency dependent term, f^{-m}, in our model, see Eq. (1). This is a simplified approach since, in real scenarios, each received pulse can have its own decay exponent [29]; nevertheless since these individual exponents are difficult to estimate we opt for a general decay exponent as in [10]. In order to estimate the value of m, we calculated the exponent of each individual frequency response and averaged over that ensemble which resulted in $m = 0.95$. This is in line with the results found in [10] and [9].

It is important to make clear that the introduction of the f^{-m} term to model all the MPCs deviates from the physical reality that each component shows different distortion. In any case, the impact of this approximation is within the clusters (i.e., the difference between the estimated MPCs considering the frequency-flat and f^{-m} assumptions, is only sizeable within clusters), and thus has a minor impact on the extracted parameters.

IV. BUILDING THE IMPULSE RESPONSE

In this section we provide step-by-step instructions on how to implement the proposed channel model. All the necessary parameters and corresponding estimated values are given in Table I, for random parameters, and in Table II, for deterministic parameters.

Since the virtual array used in the channel measurements was 8.11 m long, the model is only valid for MS positions covering distances up to this length. Similarly, the distance between BS and MS must be within 2 to 19 m. Figures 8 and 9, illustrate an example of a geometrical map and the corresponding channel impulse responses, respectively. The figures were generated using the same parameters as used in the measurements, e.g., same number of MS positions and separation distance between them. In the mathematical formulations given below, n indexes a given MS position (a "cross" in Fig. 8) and k indexes a specific scatterer (a "point" in Fig. 8). The model can then be built has follows

a) Choose the distance of the center MS with respect to the origin (BS) $d_{BS:MS}$, from a uniform distribution. Place the MS positions covering up to 8.11 m.

b) Choose the number of clusters N_{cl} from a Poisson distribution and add one (the BS cluster) to the result. For each, choose a corresponding number of scatterers N_{sc}, from a discrete Gaussian distribution.

c) Place the cluster center locations, (x_c, y_c), according to a uniform distribution within an ellipsoid, (2).

d) Position the scatterers within a cluster ensuring that their coordinates, (x_{s_k}, y_{s_k}), follow a 2D Laplacian distribution, (3).

e) For the case of scatterers belonging to *non-BS clusters*, define their contribution over the n-th MS position by,

$$S_{n,k}(f) = \sqrt{P_{\mathrm{PL}}(d_{t:s_k:r_n})p_{s_k}} \cdot \frac{V_k(\phi_n)}{V_{\mathrm{norm},k}} \cdot e^{-j(2\pi f \tau_{n,k}+\rho_k)}, \quad (13)$$

where $P_{\mathrm{LS}}(d_{t:s_k:r_n})$, (4), is the path-loss power calculated from the total propagation distance, p_{s_k} is the log-normally distributed total scatterer power, $V_k(\phi_n)$, (5), is the Gaussian shaped radiation pattern of the cluster owning the scatterer, $V_{\mathrm{norm},k}$ is a normalization variable that must be calculated to ensure that $V_k(\phi_n)$ does not scale the scatterer's total power, $\tau_{n,k}$ is the propagation delay through the scatterer assuming propagation at the speed of light c, and ρ_k is scatterer's phase, uniformly distributed from 0 to 2π.

f) For the case of scatterers belonging to the *BS cluster*, define their contribution over the n-th MS position by,

$$S_{n,k}(f) = \sqrt{P_{\mathrm{PL}}(d_{t:s_k:r_n})p_{s_k}} \cdot M(\varphi_n) \cdot e^{-j(2\pi f \tau_{n,k}+\rho_k)}. \quad (14)$$

In this case, the radiation pattern is replaced by the shadow mask $M(\varphi_n)$ (6). This can be seen from Fig. 8 by comparing the radiation of each cluster clusters (the red lines).

g) Define the LOS component (which does not include any interaction with scatterers) by

$$S_{\mathrm{LOS},n}(f) = \sqrt{P_{\mathrm{LOS}}(d_{t:r_n})} \cdot M(\varphi_n) \cdot e^{-j2\pi f \tau_{\mathrm{LOS},n}}, \quad (15)$$

where $P_{\mathrm{LOS}}(d_{t:r_n})$, (7), is the LOS power at antenna distance $d_{t:r_n}$ and $\tau_{\mathrm{LOS},n}$ is the LOS propagation delay.

h) Determine the contribution DMC by,

$$D_n(\tau) = \sqrt{D_{\mathrm{LS},n}(\tau)} \cdot D_{\mathrm{SS}}(\tau) \cdot e^{j\theta_{\mathrm{DMC}}} \quad (16)$$

where $D_{\mathrm{LS},n}(\tau)$, (8), is the large-scale deterministic diffuse power, $D_{\mathrm{SS}}(\tau)$ is the Weibull distributed small-scale variations of the DMC envelope, and θ_{DMC} is the uniformly and independently distributed tap phase. The definition of $D_{\mathrm{SS}}(\tau)$ and θ_{DMC} is based on a uniform discretization of the delay domain, $\tau = 0, \delta t, 2\delta t, \ldots$, where δt is the inverse of the system bandwidth. Its frequency domain representation can be calculated by the Fourier transform operation,

$$D'_n(f) = \mathcal{F}\{D_n(\tau)\}. \quad (17)$$

i) Finally, add together all the above components, and apply the frequency dependency term, to get the complete channel frequency response,

$$H_n(f) = \left(S_{\mathrm{LOS},n}(f) + \sum_k S_{n,k}(f) + D'_n(f) \right) \frac{f^{-m}}{F}. \quad (18)$$

Applying a Fourier transform to (18) results in the (time domain) impulse response of the channel, which is depicted in Fig. 9. The effect of shadow and visibility regions is clearly visible from the figure.
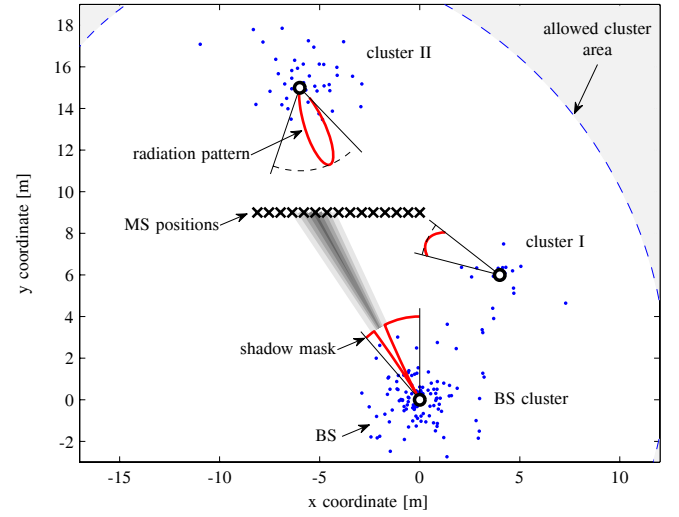

Fig. 8. Geometrical map from one specific channel model realization. The radiation patterns are positioned on the centroids of the corresponding clusters. For clarity, only 15 of the 170 MS positions are shown.
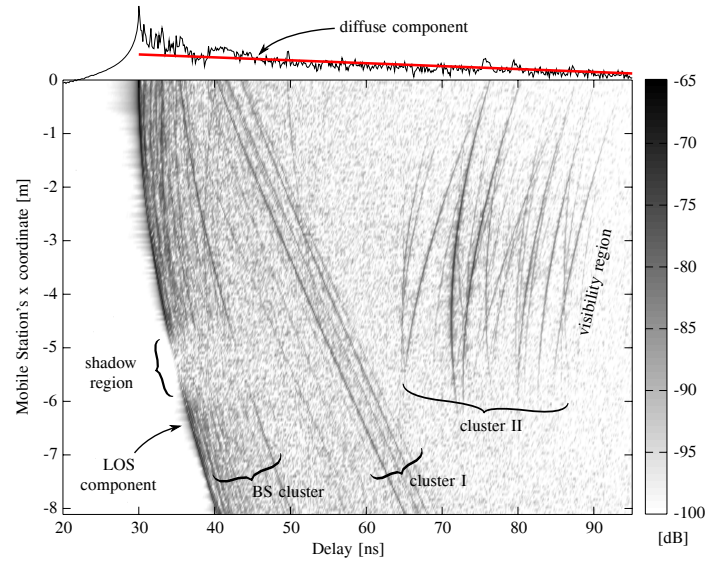

Fig. 9. Simulated channel based on the geometrical map given in Fig. 8. The main model components are identified. The figure compromises 170 impulse responses, each separated by 0.048 m.

V. MODEL VALIDATION

The validation is an important step in any model development. Here, we validate the proposed model based in two distinct approaches. First, we show that parameters derived from the model (but not directly used to parameterize it) agree well with the equivalent parameters directly computed from the measurements. An example of this is the rms delay spread, τ_{rms}, which is plotted in Fig. 10. Measured and simulated lines do not agree completely but there is a reasonably good match in terms of sample mean and sample variance. As a comparison with existing models, we find that our mean τ_{rms} of 25 ns, is in accordance with the 29 ns τ_{rms} calculated from the standardized channel model IEEE 802.15.4a CM5 for outdoor LOS [9].

Second, we investigate whether the model might be suitable to describe a general gas station scenario. In order to do so, we compare the estimated parameters from the two different mea-

TABLE I
LIST OF ALL RANDOM PARAMETERS.

Random Variable	Symbol	Unit	Distribution	Reference	Cluster Type	Parameter Values
Distance between BS and center MS	$d_{\text{BS:MS}}$	m	uniform	[13, 4-46]	−	$a = 2$ $b = 19$
No. of clusters	N_{cl}	#	Poisson	[13, 4-57]	non-BS	$\lambda = 3.25$
No. of scatterers within a cluster	N_{sc}	#	*discrete* Gaussian	[13, 4-25]	BS	$\mu = 115$ $\sigma^2 = 2190$; $N_{sc} \geq 0$
					non-BS	$\mu = 26$ $\sigma^2 = 479$; $N_{sc} \geq 0$
Cluster coordinates	(x_c, y_c)	m	2-D uniform	(2)	non-BS	$\tau_{c,max} = 1.28 \cdot 10^{-7}$
Scatterer coordinates within a cluster	(x_s, y_s)	m	2-D Laplace	(3)	BS	$\kappa = 1.43$
					non-BS	$\kappa = 2.21$
Scatterer local power variations	p_s	dB	Gaussian	[13, 4-25]	all	$\mu = 17.66$ $\sigma^2 = 32.10$
Visibility radiation pattern direction	ϕ_0	rad	uniform	[13, 4-46]	non-BS	$a = \phi_{\min}$ $b = \phi_{\max}$ (Fig. 3)
Visibility radiation pattern width	ν	rad	log-normal	[13, 5-30]	non-BS	$\mu = -0.33$ $\sigma^2 = 0.67$
No. of shadow regions (8 m array)	$N_{sh,8}$	#	Poisson	[13, 4-57]	BS	$\lambda = 1.27$
Shadow region direction	φ_0	rad	uniform	[13, 4-46]	BS	$a = \varphi_{\min}$ $b = \varphi_{\max}$ (Fig. 4)
DMC small-scale envelope variations	D_{SS}		Weibull	[13, 4-43]	−	$\alpha =$ Eq. (12) $\beta =$ Eq. (11) $u = 1.25$ $v = 3.7 \cdot 10^7$
DMC tap phase	θ_{DMC}	rad	uniform	[13, 4-46]	−	$a = 0$ $b = 2\pi$
Scatterer phase	ρ	rad	uniform	[13, 4-46]	−	$a = 0$ $b = 2\pi$

TABLE II
LIST OF ALL DETERMINISTIC PARAMETERS.

Deterministic Variable	Symbol	Unit	Reference	Cluster Type	Values/Parameters
No. of MS positions	N_{MS}	#		−	170
Distance between MS positions	Δd_{MS}	m		−	0.048
No. of frequency points	N_f	#		−	1601
Minimum frequency	$f_{\min}$	Hz		−	$3.1 \cdot 10^9$
Maximum frequency	$f_{\max}$	Hz		−	$10.6 \cdot 10^9$
Frequency step/resolution	δf	Hz		−	$4.69 \cdot 10^6$
Delay step/resolution	δt	s		−	$133.3 \cdot 10^{-9}$
Propagation speed	c	m/s		−	$3 \cdot 10^8$
Shadow region loss coefficient	a		(6)	BS	0.062
Shadow region width	$\Delta\varphi$	rad	(6)	BS	0.11
Scatterers' power path-loss	$P_{\text{PL}}(d_{t:s:r})$		(4)	all	$P_0 = 1.74 \cdot 10^{-8}$ $n_{\text{PL}} = 1.1$ $d_0 = 1$; $d_{t:s:r} \geq d_0$
Power of LOS component	$P_{\text{LOS}}(d_{t:r})$		(7)	−	$P_0 = 3.20 \cdot 10^{-6}$ $n_{\text{LOS}} = 1.69$ $d_0 = 1$; $d_{t:r} \geq d_0$
Power of DMC at LOS	$D_{\tau_{\text{LOS}}}(d_{t:r})$		(9)	−	$D_0 = 1.65 \cdot 10^{-9}$ $n_{\text{D}} = 1.18$ $d_0 = 1$; $d_{t:r} \geq d_0$
rms delay spread of DMC	$\tau_{\text{RMS}}(d_{t:r})$		(10)	−	$\tau_0 = 4.09 \cdot 10^{-8}$ $n_{\text{RMS}} = 0.17$ $d_0 = 1$; $d_{t:r} \geq d_0$
Frequency decay exponent	m		(18)	−	0.95

sured gas stations. Fig. 1 and 5 present estimated parameters when using the data from each scenario. Lastly, in Fig. 10 we also added the delay spreads of our model applied separately to scenario 1 and 2. They do not differ significantly, which supports the idea that this model has a general applicability for these kind of scenarios, though clearly a larger number of gas stations would have to be measured to provide statistically significant confirmation of this conjecture.

VI. CONCLUSIONS

In this paper, we have specified one of the few existing UWB channel models for outdoor scenarios. The aim here was to characterize the static channel, however, real situations will often include moving vehicles and people, which can result in additional time/space varying clusters of scatterers and/or shadow regions. While not including these channel effects, our model is well prepared to integrate them since it has a geometric-stochastic basis (e.g. a car could be described

by a moving cluster in our geometrical space with varying radiation properties). Such improvements would also require further measurements and possibly more complex detection algorithms.

Besides the importance of this work for infostation systems, a number of modeling concepts were also introduced: (i) cluster radiation patterns defining the cluster's visibility region, and (ii) shadowing regions that represent the large-scale attenuation of the LOS for certain TX/RX locations. These concepts were found to be of great help for the modeling of the outdoor UWB channel and it is of interest to verify if the same holds true for indoor UWB or even for narrow-band channels.
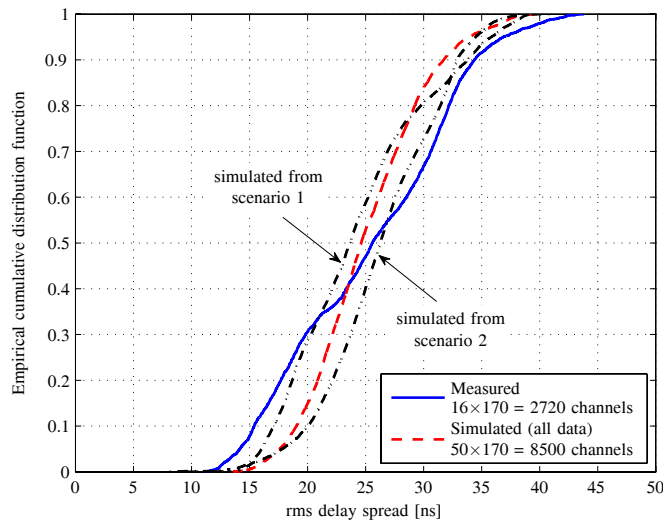
Fig. 10. CDFs of the rms delays spreads of both the measured and simulated impulse responses. The two "arrow indicated" lines correspond to the rms delay spreads calculated from the proposed channel model based separately in the data from scenario 1 and 2.

REFERENCES

[1] R. Frenkiel, B. Badrinath, J. Borres, and R. Yates, "The infostations challenge: balancing cost and ubiquity in delivering wireless data," *IEEE Personal Commun.*, vol. 7, no. 2, pp. 66–71, 2000.

[2] T. Santos, J. Karedal, P. Almers, F. Tufvesson, and A. F. Molisch, "Modeling the ultra-wideband outdoor channel—measurements and parameter extraction method," *IEEE Trans. Wireless Commun.*, vol. 9, no. 1, Jan. 2010.

[3] A. F. Molisch, "Ultrawideband propagation channels-theory, measurement, and modeling," *IEEE Trans. Veh. Technol.*, vol. 54, no. 5, pp. 1528–1545, Sep. 2005.

[4] ——, "Ultrawideband propagation channels and their impact on system design," in *Proc. Int. Symp. on Microwave, Antenna, Propag. and EMC Technol. for Wireless Commun.*, 2007, pp. K4–1–K4–5.

[5] ——, "Ultra-wide-band propagation channels," *Proc. IEEE*, vol. 97, no. 2, pp. 353–371, 2009.

[6] D. Cassioli, M. Z. Win, and A. F. Molisch, "The ultra-wide bandwidth indoor channel: from statistical model to simulations," *IEEE J. Sel. Areas Commun.*, vol. 20, no. 6, pp. 1247–1257, 2002.

[7] S. Ghassemzadeh, L. Greenstein, T. Sveinsson, A. Kavcic, and V. Tarokh, "UWB delay profile models for residential and commercial indoor environments," *IEEE Trans. Veh. Technol.*, vol. 54, no. 4, pp. 1235–1244, July 2005.

[8] A. F. Molisch, J. R. Foerster, and M. Pendergrass, "Channel models for ultrawideband personal area networks," *IEEE Trans. Wireless Commun.*, vol. 10, no. 6, pp. 14–21, Dec. 2003.

[9] A. F. Molisch, D. Cassioli, C.-C. Chong, S. Emami, A. Fort, B. Kannan, J. Karedal, J. Kunisch, H. G. Schantz, K. Siwiak, and M. Z. Win, "A comprehensive standardized model for ultrawideband propagation channels," *IEEE Trans. Antennas Propag.*, vol. 54, no. 11, pp. 3151–3166, Nov. 2006.

[10] J. Kunisch and J. Pamp, "An ultra-wideband space-variant multipath indoor radio channel model," in *Proc. IEEE Conf. Ultra Wideband Syst. Technol. Digest Techn. Papers*, 2003, pp. 290–294.

[11] A. Domazetovic, L. J. Greenstein, N. B. Mandayam, and I. Seskar, "A new modeling approach for wireless channels with predictable path geometries," in *Proc. IEEE Veh. Technol. Conf. (VTC'02–Fall)*, vol. 1, Sep. 2002, pp. 454–458.

[12] Y. Chen and V. Dubey, "An azimuth-frequency domain geometric model for ultrawide bandwidth signal propagation," in *Springer Wireless Personal Commun.*, vol. 31, Oct. 2004, pp. 1–18.

[13] A. Papoulis and S. U. Pillai, *Probability, Random Variables and Stochastic Processes*, 4th ed. McGraw Hill, 2002.

[14] U. G. Schuster, "Wireless communication over wideband channels," Ph.D. dissertation, Series in Communication Theory, ISSN 1865-6765, Germany, 2009.

[15] N. Czink, P. Cera, J. Salo, E. Bonek, J.-P. Nuutinen, and J. Ylitalo, "A framework for automatic clustering of parametric MIMO channel data

[16] J. Fuhl, A. Molisch, and E. Bonek, "Unified channel model for mobile radio systems with smart antennas," in *IEE Proc. Radar, Sonar Navig.*, vol. 145, no. 1, 1998, pp. 32–41.

[17] G. Schuster and H. Bölcskei, "Ultra-wideband channel modeling on the basis of information-theoretic criteria," *IEEE Trans. Wireless Commun.*, pp. 2464–2475, July 2007.

[18] H. Akaike, "Likelihood of a model and information criteria," *J. Econometrics*, vol. 16, no. 1, pp. 3–14, 1981.

[19] T. Eltoft, T. Kim, and T.-W. Lee, "On the multivariate Laplace distribution," *IEEE Signal Process. Lett.*, vol. 13, no. 5, pp. 300–303, May 2006.

[20] A. F. Molisch, *Wireless Communications*. John Wiley, 2005.

[21] M. Steinbauer, A. F. Molisch, and E. Bonek, "The double-directional radio channel," *IEEE Antennas Propag. Mag.*, vol. 43, no. 4, pp. 51–63, 2001.

[22] A. F. Molisch, H. Asplund, R. Heddergott, M. Steinbauer, and T. Zwick, "The COST259 directional channel model part I: overview and methodology," *IEEE Trans. Veh. Commun.*, vol. 5, no. 12, pp. 3421–3433, Dec. 2006.

[23] H. Asplund, A. A. Glazunov, A. F. Molisch, K. I. Pedersen, and M. Steinbauer, "The COST259 directional channel model—part II: macrocells," *IEEE Trans. Wireless Commun.*, vol. 5, no. 12, pp. 3434–3450, 2006.

[24] Y. Chen and V. K. Dubey, "Visibility of far clusters in directional mobile radio channels," *IEEE Commun. Lett.*, vol. 7, no. 9, pp. 422–424, 2003.

[25] A. Richter, "Estimation of radio channel parameters: models and algorithms," Ph.D. dissertation, Technische Universität Ilmenau, Ilmenau, 2005.

[26] L. J. Greenstein, V. Erceg, Y. S. Yeh, and M. V. Clark, "A new path-gain/delay-spread propagation model for digital cellular channels," *IEEE Trans. Veh. Technol.*, vol. 46, no. 2, pp. 477–485, 1997.

[27] J. Cheng and N. Beaulieu, "Maximum-likelihood based estimation of the Nakagami m parameter," *IEEE Commun. Lett.*, vol. 5, no. 3, pp. 101–103, 2001.

[28] N. Balakrishnan and M. Kateri, "On the maximum likelihood estimation of parameters of Weibull distribution based on complete and censored data," *Statistics & Probability Letters*, vol. 78, no. 17, pp. 2971–2975, 2008.

[29] R. Qiu and I.-T. Lu, "Wideband wireless multipath channel modeling with path frequency dependence," in *Proc. IEEE Int. Conf. Commun.*, vol. 1, 1996, pp. 277–281.

Telmo Santos received his M.S. degree in electronics and computer engineering in 2005 from Coimbra University, Portugal, and his Licentiate degree in wireless communications in 2009, from Lund University, Sweden. He is currently a Ph.D. student at the Department of Electrical and Information Technology, Lund University, where his main research interests concern measurements and modeling of wireless propagation channels for UWB systems and waterfilling gains and antenna selection schemes for MIMO systems. In addition, he is also interested in the simulation and real-time implementation of MIMO-OFDM communication systems. Before enrolling on his Ph.D. studies he was employed at Critical Software in Portugal, where he worked mainly with real-time operative systems with the Department of Embedded and Dependability.

Fredrik Tufvesson was born in Lund, Sweden in 1970. He received the M.S. degree in electrical engineering in 1994, the Licentiate Degree in 1998 and his Ph.D. in 2000, all from Lund University in Sweden. After almost two years at a startup company, Fiberless Society, Fredrik is now associate professor at the Department of Electrical and Information Technology. His main research interests are channel measurements and modeling for wireless communication, including channels for both MIMO and UWB systems. Beside this, he also works with channel estimation and synchronization problems, OFDM system design and UWB transceiver design.

Andreas F. Molisch received the Dipl. Ing., Dr. techn., and habilitation degrees from the Technical University Vienna (Austria) in 1990, 1994, and 1999, respectively. From 1991 to 2000, he was with the TU Vienna, becoming an associate professor there in 1999. From 2000-2002, he was with the Wireless Systems Research Department at AT&T (Bell) Laboratories Research in Middletown, NJ. From 2002-2008, he was with Mitsubishi Electric Research Labs, Cambridge, MA, USA, most recently as Distinguished Member of Technical Staff and Chief Wireless Standards Architect. Concurrently he was also Professor and Chairholder for radio systems at Lund University, Sweden. Since 2009, he is Professor of Electrical Engineering at the University of Southern California, Los Angeles, CA, USA.

Dr. Molisch has done research in the areas of SAW filters, radiative transfer in atomic vapors, atomic line filters, smart antennas, and wideband systems. His current research interests are measurement and modeling of mobile radio channels, UWB, cooperative communications, and MIMO systems. Dr. Molisch has authored, co-authored or edited four books (among them the textbook *Wireless Communications*, Wiley-IEEE Press), eleven book chapters, more than 110 journal papers, and numerous conference contributions, as well as more than 70 patents and 60 standards contributions.

Dr. Molisch is Area Editor for Antennas and Propagation of the IEEE TRANSACTIONS ON WIRELESS COMMUNICATIONS and co-editor of special issues of several journals. He has been member of numerous TPCs, vice chair of the TPC of VTC 2005 spring, general chair of ICUWB 2006, TPC co-chair of the wireless symposium of Globecomm 2007, TPC chair of Chinacom2007, and general chair of Chinacom 2008. He has participated in the European research initiatives "COST 231," "COST 259," and "COST273," where he was chairman of the MIMO channel working group, he was chairman of the IEEE 802.15.4a channel model standardization group. From 2005-2008, he was also chairman of Commission C (signals and systems) of URSI (International Union of Radio Scientists), and since 2009, he is the Chair of the Radio Communications Committee of the IEEE Communications Society. Dr. Molisch is a Fellow of the IEEE, a Fellow of the IET, an IEEE Distinguished Lecturer, and recipient of several awards.